

SOLAR PHYSICS

Observing the evolution of the Sun's global coronal magnetic field over 8 months

Zihao Yang^{1,2}, Hui Tian^{1,3*}, Steven Tomczyk^{2,4}, Xianyu Liu^{1,5}, Sarah Gibson², Richard J. Morton⁶, Cooper Downs⁷

The magnetic field in the Sun's corona stores energy that can be released to heat plasma and drive solar eruptions. Measurements of the global coronal magnetic field have been limited to several snapshots. In this work, we present observations, using the Upgraded Coronal Multi-channel Polarimeter, that provide 114 magnetograms of the global corona above the solar limb spanning ~8 months. We determined the magnetic field distribution with altitude in the corona and monitored the evolution at different latitudes over multiple solar rotations. The field strength between 1.05 and 1.60 solar radii varies from <1 to ~20 gauss. A signature of active longitudes appears in the coronal magnetic field measurements. Coronal models are generally consistent with our observations, though they have larger discrepancies in high-latitude regions.

The magnetic field plays a dominant role in many physical processes that occur on the Sun, including transient solar eruptions, plasma heating, and the 11-year solar activity cycle. Understanding these phenomena requires measurements of the evolving magnetic field at all altitudes in the Sun's atmosphere (1–3). Magnetic fields on the Sun's visible surface (the photosphere) are routinely measured using the Zeeman effect—the splitting of some spectral lines owing to the presence of an external magnetic field. However, it is difficult to extend such measurements to the Sun's upper atmosphere, particularly the corona, because of the much weaker emission and smaller line splitting. The coronal magnetic field is the source of energy that heats the hot plasma in the corona (4) and drives intermittent solar eruptions (5), but no routine measurements are available of the magnetic field in the corona.

Some individual measurements of the coronal magnetic field have been made through a variety of methods. For example, spectropolarimetric measurements of infrared spectral lines have been used to determine the magnetic fields in specific regions of the corona with very strong field (6–8). Radio spectral imaging observations have been used to estimate coronal magnetic field strengths in flaring regions (9–11). A predicted relationship between the intensity of the Fe x 25.7-nm ultraviolet

spectral line and the magnetic field strength (12) has been proposed as a means to measure the coronal magnetic field (13); however, existing instruments lack the precision required by that technique (14). Coronal seismology has been used to infer magnetic field strengths from observations of magnetohydrodynamic (MHD) waves in the corona (15–17). However, this technique is usually applied to single-oscillation events, which provide only a single value for the field strength within an oscillating structure. None of these techniques have been routinely implemented to monitor the evolution of the Sun's global coronal magnetic field.

Coronal seismology has also been applied to propagating transverse MHD waves (18, 19), which are more pervasive in the corona than individual transient oscillations. Observations of the corona above the solar limb (beyond the solar disk as seen from Earth) using the Coronal Multi-channel Polarimeter (CoMP) (20) have been used to produce individual global coronal magnetograms (maps of magnetic field strength and direction) (21, 22). This two-dimensional (2D) coronal seismology technique provides maps of the plane-of-sky (POS) component of the global coronal magnetic field. However, owing to the limited signal-to-noise ratio (S/N), only a few CoMP datasets have been used to generate global magnetograms. Routine monitoring would require approximately daily measurements of the coronal magnetic field.

Observations of the corona

We analyzed observations of the corona with the Upgraded Coronal Multi-channel Polarimeter (UCoMP) (23). Daily scientific observations with UCoMP began in mid-2021. After completion of instrument commissioning, the data quality stabilized in early 2022. Observations were performed almost daily from that point until they were halted in late November 2022 by a volcanic eruption of Mauna Loa (UCoMP is

located on the slopes of that mountain). UCoMP provides imaging spectral observations of the above-limb corona at all latitudes. Compared with CoMP, it has an expanded field of view (FOV) covering ~1.05 to 1.60 solar radii, a higher spatial resolution of ~6", higher sensitivity, and improved data quality stability.

UCoMP performs imaging spectroscopy by recording a spectrum at each pixel within the FOV, targeting the Fe xiii 1074.7-nm and 1079.8-nm near-infrared spectral lines. Each spectral profile was fitted with a Gaussian function to determine the line intensity and Doppler velocity of the coronal plasma at each location within the FOV (24). The intensity ratio of the two lines was used to map the electron number density (and therefore the plasma mass density, assuming overall neutral charge) in the corona (21, 22).

Previous observations with CoMP have shown prevalent propagating disturbances in the Doppler velocity maps of Fe xiii 1074.7 nm, which were interpreted as being due to propagating transverse MHD waves, called kink waves (18, 19, 21). Similar evidence for kink waves is present in the UCoMP data (movie S1). We modified (25) a previous wave tracking technique (26) and applied it to the UCoMP observations to determine the wave propagation direction and phase speed at each pixel within the FOV.

The data quality of the UCoMP observations was sufficient for us to derive maps of plasma density, wave propagation direction, and phase speed in the global corona for 114 days during the 253-day (~8-month) period of 19 February to 29 October 2022. Most data gaps are attributable to bad weather conditions. This period spanned more than nine rotations of the Sun (Carrington rotations, with a period of ~27.27 days). By contrast, previous CoMP observations provided usable maps on only 1 or 2 days per year (21, 22).

Determining the coronal magnetic field

Using the density diagnostics and wave tracking results, we applied 2D coronal seismology to determine global maps of the coronal magnetic field (21, 22). Under the condition of magnetic pressure dominance (which applies in the corona) and at UCoMP's resolution of ~6", the magnetic field strength is related to the local plasma density and phase speed of the observed kink wave as (17, 25, 27)

$$B = v_{ph} \sqrt{\mu_0 \rho} \quad (1)$$

where B is the magnetic field strength, ρ is the plasma density, v_{ph} is the wave phase speed, and μ_0 is the magnetic permeability in a vacuum. Because the corona is optically thin (minimal attenuation) to the Fe xiii lines at 1074.7 nm and 1079.8 nm, the observed spectral profiles are integrations of the line emission along the line of sight (LOS). Therefore, the

¹School of Earth and Space Sciences, Peking University, Beijing 100871, People's Republic of China. ²High Altitude Observatory, National Center for Atmospheric Research, Boulder, CO 80307, USA. ³Key Laboratory of Solar Activity and Space Weather, National Space Science Center, Chinese Academy of Sciences, Beijing 100190, People's Republic of China. ⁴Solar Scientific LLC, Boulder, CO 80301, USA. ⁵Department of Climate and Space Sciences and Engineering, University of Michigan, Ann Arbor, MI 48109, USA. ⁶Department of Mathematics, Physics and Electrical Engineering, Northumbria University, Newcastle Upon Tyne NE1 8ST, UK. ⁷Predictive Science Inc., San Diego, CA 92121, USA.

*Corresponding author. Email: hui.tian@pku.edu.cn

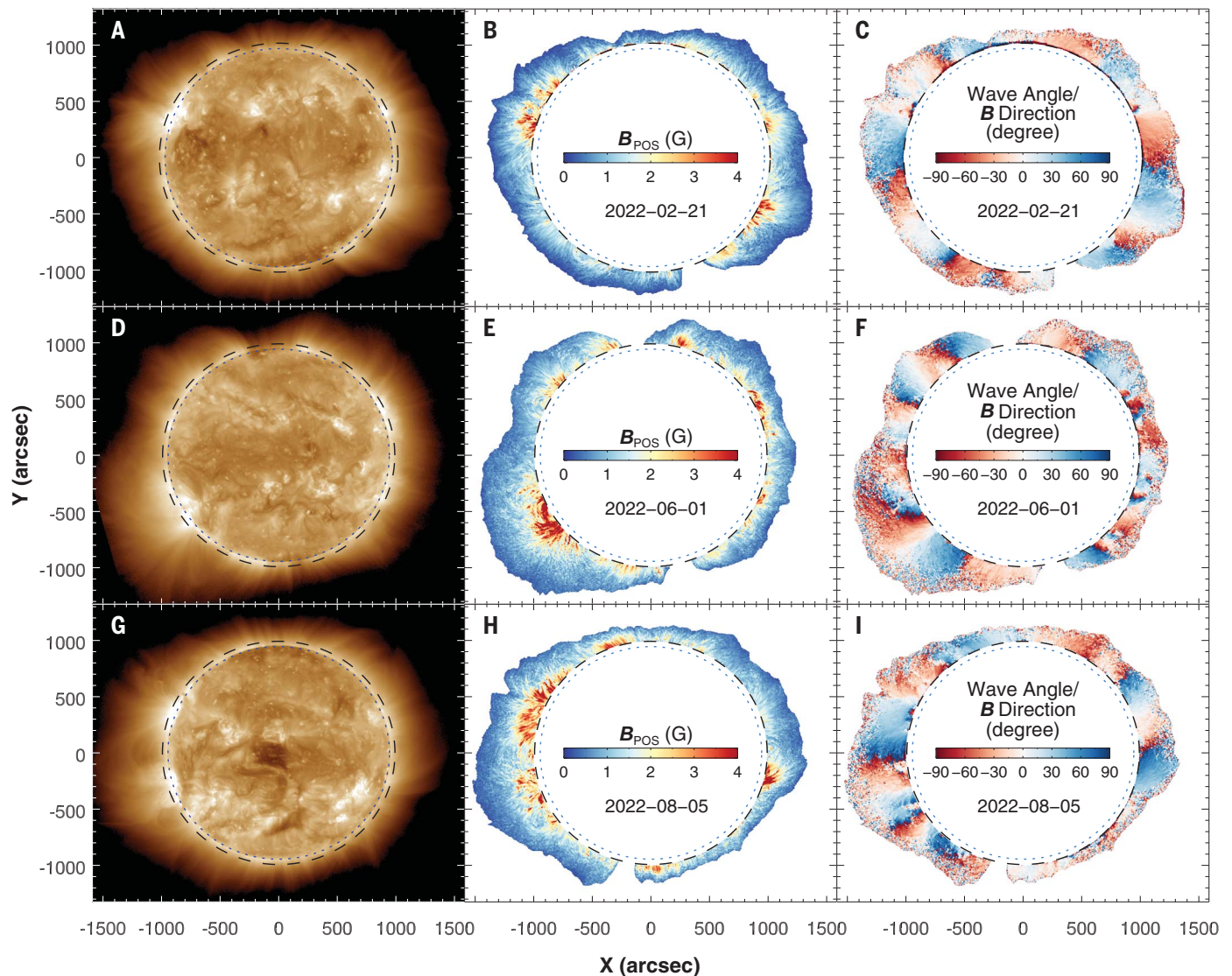


Fig. 1. Three example global coronal magnetic field maps and corresponding ultraviolet images. In all panels, the x axis is the east-west direction and the y axis is the north-south direction; their zero point is the center of the solar disk. The dotted and dashed circles mark the edge of the solar disk (limb) and the inner boundary of the UCoMP FOV, respectively. **(A)** High-dynamic range SUVI image of 19.5-nm emission intensity (25) from 19:48 to 19:52 UT on 21 February 2022. **(B)** UCoMP map of the coronal POS magnetic field strength (color bar) on 21 February 2022 (labeled in year-month-day format). A median filter of 3 pixels by 3 pixels has been applied to reduce noise. Central blank parts are because of obscuration by the coronagraph occulter,

and blank parts in the outer regions are pixels with insufficient S/N. **(C)** Same as (B), but for the magnetic field direction projected onto the POS. Angles are measured with respect to the local radial direction. Positive angles are counterclockwise, and negative angles are clockwise. **(D)** Same as (A), but for 20:48 to 20:52 UT on 1 June 2022. **(E and F)** Same as (B) and (C), respectively, but for 1 June 2022. **(G)** Same as (A), but for 19:48 to 19:52 UT on 5 August 2022. **(H and I)** Same as (B) and (C), respectively, but for 5 August 2022. The uncertainties on the measured magnetic field strength and direction are shown in figs. S2 and S3, respectively. Corresponding maps for all 114 datasets are shown in movie S2.

magnetic field strength derived using Eq. 1 is a weighted average along the LOS.

We applied Eq. 1 to the UCoMP global maps of plasma density and wave phase speed to produce 114 global maps of the coronal magnetic field (movie S2). Figure 1 shows three examples of our results on 21 February, 1 June, and 5 August 2022, along with simultaneous coronal images at 19.5 nm for comparison from the Solar UltraViolet Imager (SUVI) (28) on the Geostationary Operational Environmen-

tal Satellite. The magnetic field strengths in the UCoMP FOV are mostly in the range of 0.5 to 4 G. In some cases, at low altitudes above active regions (regions with strong 19.5-nm emission), the coronal field that we inferred reaches ~20 G. We estimated the uncertainties on these field strengths to be generally <20% (25).

Because the measured wave phase speeds are only the projection of the true speeds onto the POS, perpendicular to the LOS, the mea-

sured field strengths are the POS component of the coronal magnetic field (21). Kink waves propagate along magnetic field lines, so the inferred wave propagation directions indicate the coronal magnetic field directions projected onto the POS (22). Therefore, our global maps represent both the strength and direction of the coronal magnetic field projected onto the POS. The UCoMP observations provided global coronal magnetograms with an average frequency of approximately once every 2 days.

Evolution of the coronal magnetic field

Previous mapping of the global coronal magnetic field using CoMP (21, 22) determined the field strength and direction in the height range of ~ 1.05 to 1.35 solar radii, mostly limited to

latitudes $\lesssim 50^\circ$. The UCoMP maps extend that coverage to higher altitudes, sometimes reaching ~ 1.6 solar radii (Fig. 1), and to nearly all latitudes, including the polar regions [albeit at lower altitudes and restricted to locations with strong

signals (Fig. 1)]. The magnetic field in solar polar regions plays a role in the progression of solar cycles, with the field strength at solar minimum sometimes being used to predict the strength of the following solar cycle (29).

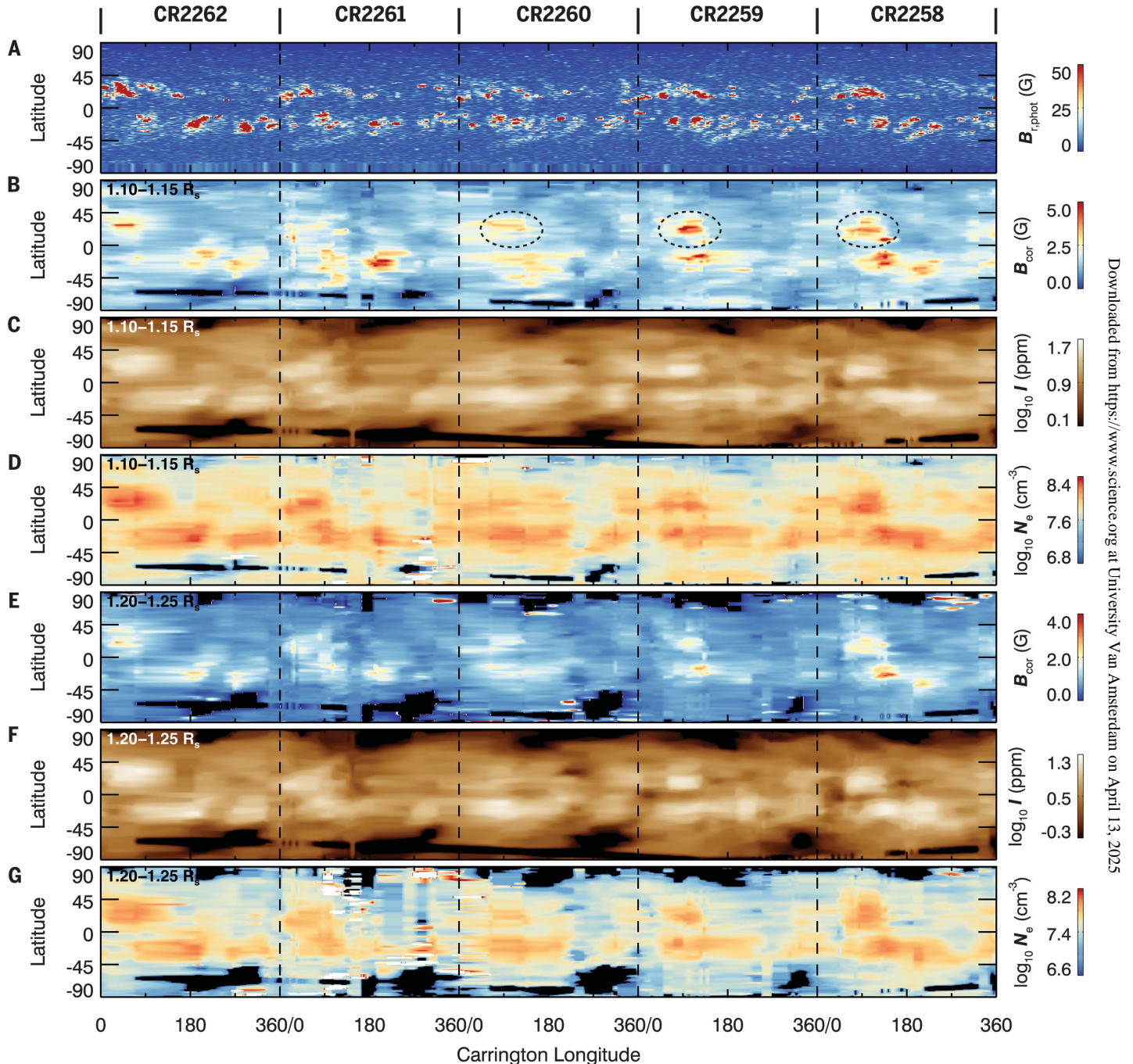


Fig. 2. Carrington maps of the photospheric and coronal magnetic fields, Fe XIII 1074.7-nm line intensity, and electron density. Time increases from right to left. The maps show each quantity (color bars) as functions of solar latitude and Carrington longitude, for five Carrington rotations (denoted CR2258 to CR2262, labeled at the top) separated by dashed vertical lines. (A) The radial component of the photospheric magnetic field strength ($B_{r,\text{phot}}$) measured by HMI. (B to D) The coronal magnetic field strength (B_{cor}) (B), Fe XIII 1074.7-nm line intensity (I) (C), and electron density (N_e) (D), each averaged between 1.10 and

1.15 solar radii (R_s). (E to G) Same as (B) to (D), respectively, but averaged between 1.20 and 1.25 R_s . The coronal measurements are not uniform in longitude owing to data gaps in the 114 datasets, so those Carrington maps have been interpolated to a constant angular resolution (1°) along the longitude axis, producing elongated features. The black and white areas on the maps represent regions excluded because of low S/N or anomalously high values, respectively. The black ellipses in (B) indicate the recurrence of strong coronal magnetic field at similar longitudes. ppm, parts per million.

Carrington maps show the evolution of solar properties over successive rotations of the Sun; the x axis is longitude as it rotates into view over time (reversed, such that newer data are on the left and older data on the right), and the y axis shows latitude. From the 114 global maps of coronal magnetic field strength, we constructed (25) Carrington maps of magnetic field strength and plasma density at various heights in the corona during different Carrington rotations of the Sun (Fig. 2). These maps show the evolution of the coronal magnetic field over 8 months at nearly all latitudes and across different heights as the Sun rotates. We reprojected these Carrington maps for each Carrington rotation onto a spherical coordinate system from which we extracted the magnetic field distributions in spherical shells with different radii from the solar center (movie S3). Figure 3 shows three examples of the spherical distributions in two altitude ranges: 1.10 to 1.15 and 1.20 to 1.25 solar radii. For comparison, Fig. 3 also shows the spherical distributions of the corresponding radial magnetic field on the photosphere, as measured by the Helioseismic

and Magnetic Imager (HMI) (30) on the Solar Dynamics Observatory (SDO) spacecraft. To facilitate comparison, the angular resolution of the HMI magnetic field map has been degraded to match that of the UCoMP coronal maps (25).

We identified a pattern in the magnetic field structures at different atmospheric layers: Regions with strong field in the photosphere generally show strong field in the corresponding coronal measurements (example regions labeled in Fig. 3). This coherence implies that the magnetic fields are connected between different layers of the solar atmosphere. However, we also identified localized patches of strong photospheric field that do not coincide with strong-field features in the corona (also labeled in Fig. 3). Possible explanations of this difference include strong expansion of a flux tube with height (decreasing the magnetic field at higher locations due to flux conservation) or low-lying closed magnetic structures (if magnetic field lines close at low heights and do not extend into higher layers, which produces stronger field at lower heights and weaker field at higher altitudes).

Previous observations of photospheric magnetic fields have shown that newly emerging active regions tend to appear at similar locations to previous active regions (31, 32). This behavior is related to the recurrent emergence of magnetic flux at specific longitudinal sectors, known as active longitudes. The active regions that emerged during our observational period typically did not persist for a full solar rotation (see supplementary text). The recurrence of strong-field regions at similar longitudes is visible in the coronal Carrington maps (Fig. 2, B and E), which indicates that active longitudes extend their influence into the coronal magnetic field.

Comparison with theoretical models

Previous work has used 3D MHD models to study the evolution of the coronal magnetic field and its coupling with plasma in the solar corona (33). Some models use the observed photospheric magnetic fields to predict coronal emission and magnetic field structures (33). For comparison with our LOS-integrated observations, we computed (25) coronal models using the magnetohydrodynamic algorithm

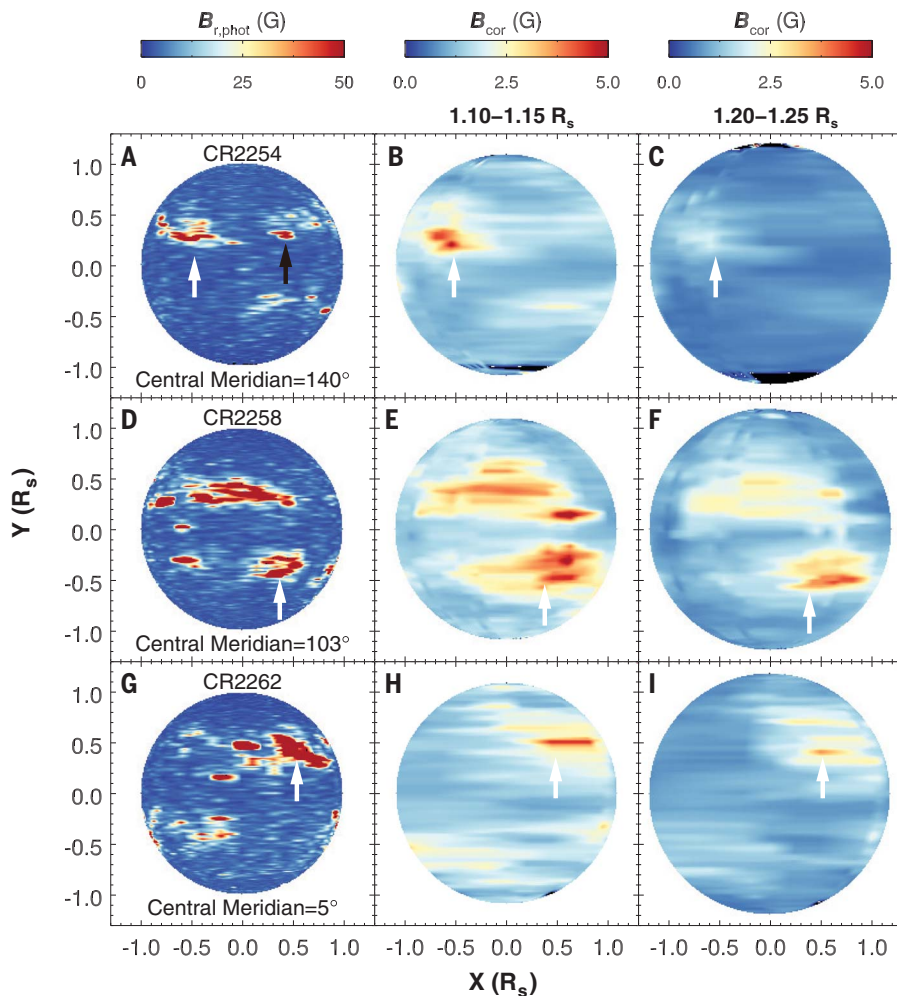
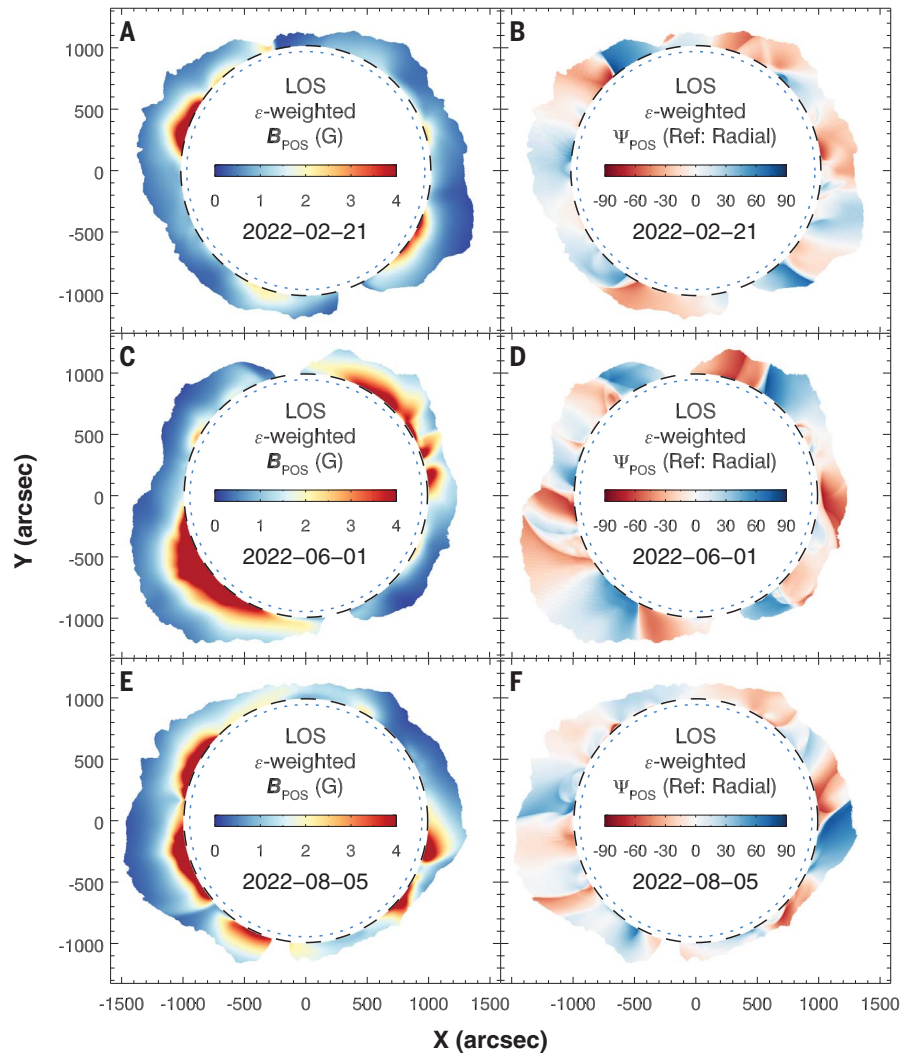


Fig. 3. Spherical distributions of the magnetic field strength in different atmospheric layers. (A) The radial photospheric magnetic field (color bar) from HMI during CR2254, projected onto a sphere with central meridian at 140° . (B) Same as (A), but for the coronal magnetic field from UCoMP averaged between 1.10 and 1.15 solar radii. (C) Same as (B), but averaged between 1.20 and 1.25 solar radii. (D to F) Same as (A) to (C), respectively, but during CR2258 and projected with a 103° central meridian. (G to I) Same as (A) to (C), respectively, but during CR2262 and projected with a 5° central meridian. Movie S3 is an animated version of this figure, showing all meridians over five Carrington rotations. The white arrows indicate strong-field regions that are coherent across different layers. The black arrow indicates a region with strong field only in the photosphere.

Fig. 4. Predictions from the MAS models. (A and B) Global maps are shown for the LOS emissivity-weighted coronal magnetic field strength (B_{POS}) (A) and the magnetic field direction (Ψ_{POS} , defined as in Fig. 1) (B) predicted by the MAS model of 21 February 2022. The label "Ref: Radial" indicates that the angles are determined with respect to the local radial direction. (C and D) Same as (A) and (B), respectively, but for the 1 June 2022 model. (E and F) Same as (A) and (B), respectively, but for the 5 August 2022 model. All of these models were constructed using the photospheric magnetic fields observed by HMI as boundary conditions (25) and were compared (supplementary text) with the corresponding UCoMP observations (Fig. 1). Color bars and line styles are the same as in Fig. 1.



outside a sphere (MAS) MHD code (34) (hereafter MAS models). We generated three MAS models using the photospheric magnetograms during three Carrington rotations (designated CR2254, CR2258, and CR2260). These three were chosen because they correspond to the observations shown in Fig. 1. From the three MAS models, we extracted the predicted POS component of the coronal magnetic field strength and direction and the Fe XIII 1074.7-nm line emissivity (the spectral energy released per unit volume per unit time) at each grid point along each LOS within the FOV. From these model data, we calculated the predicted LOS emissivity-weighted physical parameters as

$$\bar{f} = \frac{\int f_i \cdot \epsilon_i dL}{\int \epsilon_i dL} \quad (2)$$

where f_i is the physical parameter of interest (either the POS component of magnetic field strength B_{POS} or its direction Ψ_{POS}), ϵ_i is the line emissivity, i is an index labeling each location along the LOS, and dL is the differential distance along the LOS.

The resulting maps of the model-predicted LOS emissivity-weighted B_{POS} and Ψ_{POS} are shown in Fig. 4. We discuss how these maps compare with the corresponding UCoMP observations in the supplementary text. Figure 5 shows a quantitative 2D comparison between the models and observations. We found similar features in the observations and model predictions, especially in low- and mid-latitude regions (Fig. 5, A and B). This similarity suggests that the UCoMP measurements of the corona are generally consistent with being LOS emissivity-weighted, as we assumed in our analysis.

We also identified some discrepancies between the MAS models and the observations, which we attribute to the limitations and assumptions in the modeling (25). For example, the adopted MAS models have lower spatial resolutions than the observations, so they lack some observed small-scale structures (for example, the fibril-like structures in active regions in Fig. 1, B, E, and H). The photospheric magnetograms used as boundary conditions

for the models were constructed using HMI observations taken over 27 days, not specific to the days of our UCoMP observations. The discrepancies in magnetic field strengths are largest in higher-latitude regions (Fig. 5C), potentially because photospheric magnetic field measurements are less reliable at high latitudes owing to projection effects, and are missing entirely in polar regions. The discrepancies in the coronal magnetic field directions between the models and observations have less dependence on latitude. We attribute some of the discrepancies to the process of LOS emissivity-weighting of the MAS model output (supplementary text).

A comparison of our observations with the potential field source surface (PFSS) models (25) has also been made, revealing some large-scale similarities but also numerous discrepancies. These discrepancies are primarily attributable to the lack of information on plasma temperature and density as well as the assumptions inherent in the PFSS models (supplementary text).

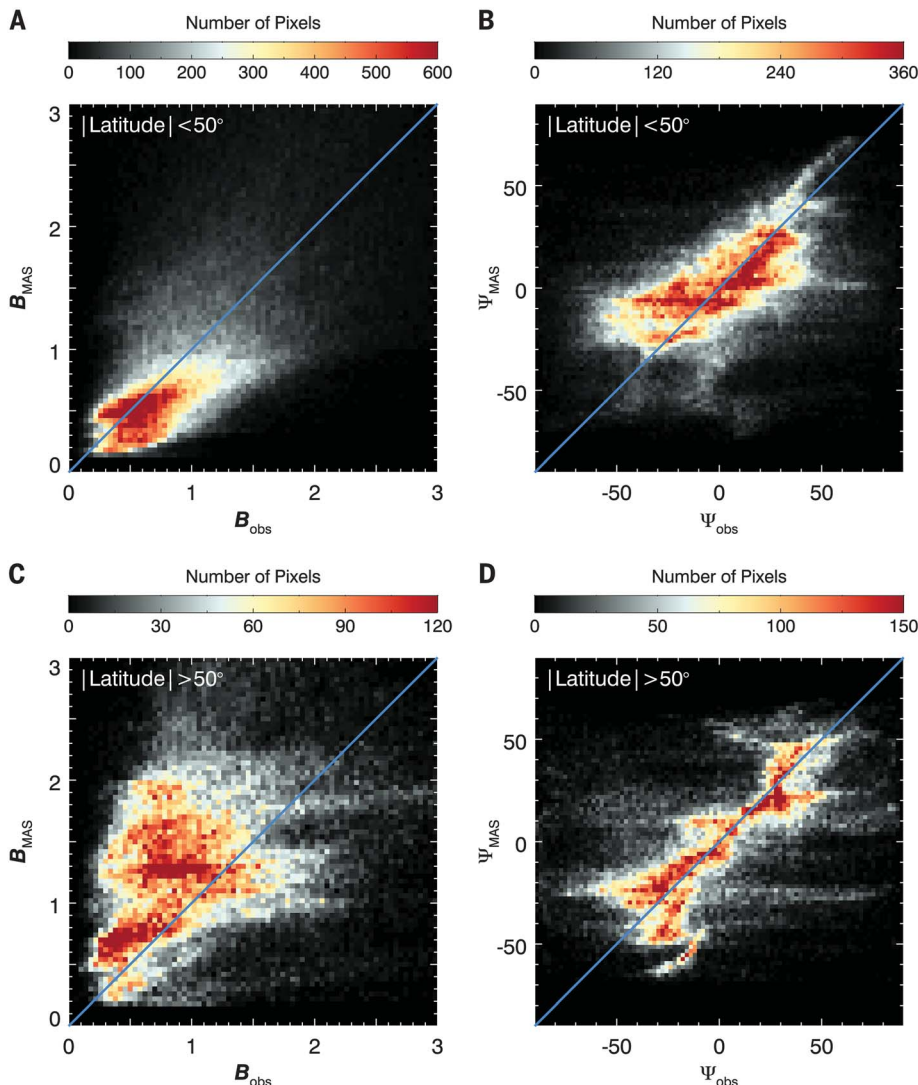


Fig. 5. Quantitative comparison between the MAS models and UCoMP observations. 2D histograms comparing the measured POS coronal magnetic field (labeled with subscripts “obs”) with the LOS emissivity-weighted magnetic field predicted by the MAS models (labeled with subscripts “MAS”). Each panel shows the number of pixels (color bar) in the maps that have each combination of magnetic field strength (B_{obs} , B_{MAS}) or direction (Ψ_{obs} , Ψ_{MAS}). The blue diagonal line indicates 1:1 correspondence. (A) Comparison of the magnetic field strengths in the models and observations for pixels at latitudes between -50° and $+50^\circ$ for the three example maps shown in Figs. 1 and 4. (B) Same as (A), but for the field direction. (C) Same as (A), but for latitudes greater than 50° in both the Southern and Northern Hemispheres. (D) Same as (C), but for the field direction. See the supplementary text for discussion.

Summary and conclusions

Our results demonstrate routine measurements of the coronal magnetic field over a period of 8 months, with an average cadence of once every 2 days. From these measurements, we generated Carrington maps of the coronal magnetic field at all latitudes, for different altitudes, and spanning multiple solar rotations. We found that the magnetic field strengths at 1.05 to 1.60 solar radii vary from <1 to ~ 20 G. A comparison with photospheric observations indicates that some strong-field regions at the photosphere are connected to strong-field regions in the

corona and others are not. A signature of active longitudes has been identified in the coronal magnetic field measurements. MHD models of the coronal magnetic field are generally consistent with our observations but do not match all the observed features, particularly at high latitudes.

REFERENCES AND NOTES

1. T. Wiegmann, J. K. Thalmann, S. K. Solanki, *Astron. Astrophys. Rev.* **22**, 78 (2014).
2. T. Samanta et al., *Science* **366**, 890–894 (2019).
3. R. Ishikawa et al., *Sci. Adv.* **7**, eabe8406 (2021).
4. S. K. Solanki, A. Lagg, J. Woch, N. Krupp, M. Collados, *Nature* **425**, 692–695 (2003).

5. P. F. Wyper, S. K. Antiochos, C. R. DeVore, *Nature* **544**, 452–455 (2017).
6. H. Lin, M. J. Penn, S. Tomczyk, *Astrophys. J.* **541**, L83–L86 (2000).
7. H. Lin, J. R. Kuhn, R. Coulter, *Astrophys. J.* **613**, L177–L180 (2004).
8. D. Kuridze et al., *Astrophys. J.* **874**, 126 (2019).
9. B. Chen et al., *Nat. Astron.* **4**, 1140–1147 (2020).
10. G. D. Fleishman et al., *Science* **367**, 278–280 (2020).
11. G. D. Fleishman, G. M. Nita, B. Chen, S. Yu, D. E. Gary, *Nature* **606**, 674–677 (2022).
12. W. Li et al., *Astrophys. J.* **807**, 69 (2015).
13. E. Landi, R. Hutton, T. Brage, W. Li, *Astrophys. J.* **904**, 87 (2020).
14. Y. Chen et al., *Astrophys. J.* **920**, 116 (2021).
15. V. M. Nakariakov, L. Ofman, *Astron. Astrophys.* **372**, L53–L56 (2001).
16. D. B. Jess et al., *Nat. Phys.* **12**, 179–185 (2015).
17. R. J. Morton, S. Tomczyk, R. Pinto, *Nat. Commun.* **6**, 7813 (2015).
18. S. Tomczyk et al., *Science* **317**, 1192–1196 (2007).
19. R. J. Morton, M. J. Weberg, J. A. McLaughlin, *Nat. Astron.* **3**, 223–229 (2019).
20. S. Tomczyk et al., *Sol. Phys.* **247**, 411–428 (2008).
21. Z. Yang et al., *Science* **369**, 694–697 (2020).
22. Z. Yang et al., *Sci. China Technol. Sci.* **63**, 2357–2368 (2020).
23. E. Landi, S. R. Habbal, S. Tomczyk, *J. Geophys. Res. Space Phys.* **121**, 8237–8249 (2016).
24. H. Tian et al., *Sol. Phys.* **288**, 637–650 (2013).
25. Materials and methods are available as supplementary materials.
26. S. Tomczyk, S. W. McIntosh, *Astrophys. J.* **697**, 1384–1391 (2009).
27. N. Magyar, T. Van Doorslaere, *Astrophys. J.* **856**, 144 (2018).
28. J. M. Darnel et al., *Space Weather* **20**, e2022SW003044 (2022).
29. D. H. Hathaway, *Living Rev. Sol. Phys.* **12**, 4 (2015).
30. P. H. Scherrer et al., *Sol. Phys.* **275**, 207–227 (2012).
31. V. Bumba, R. Howard, *Sol. Phys.* **7**, 28–38 (1969).
32. L. van Driel-Gesztelyi, L. M. Green, *Living Rev. Sol. Phys.* **12**, 1 (2015).
33. Z. Mikić et al., *Nat. Astron.* **2**, 913–921 (2018).
34. R. Lionello, J. A. Linker, Z. Mikić, *Astrophys. J.* **690**, 902–912 (2009).
35. C. Downs, Associated modeling data & materials for manuscript: Observing the evolution of the Sun’s global coronal magnetic field over eight months, Data set, Zenodo (2024); <https://doi.org/10.5281/zenodo.13351573>.
36. Z. Yang, Analysis codes for UCoMP coronal magnetic field measurement paper, Zenodo (2024); <https://doi.org/10.5281/zenodo.13367069>.

ACKNOWLEDGMENTS

We thank M. Galloy for running the UCoMP data-processing pipeline, the SDO-HMI and SUVI teams for making their data publicly available, G. de Toma for helpful discussions on data processing, and Y. Gao for helpful discussions on coronal seismology. HMI is an instrument on SDO, a mission of NASA’s Living With a Star Program. **Funding:** H.T., Z.Y., and X.L. were supported by the National Natural Science Foundation of China grant 12425301 and the National Key R&D Program of China (nos. 2021YFA0718600 and 2021YFA1600500). H.T. also acknowledges support from the New Cornerstone Science Foundation through the Xplorer Prize. R.J.M. was supported by a UKRI Future Leader Fellowship (R/PSAWMR/T019891/1). The UCoMP instrument was developed with support from the National Science Foundation (NSF) and is located at the Mauna Loa Solar Observatory, operated by the High Altitude Observatory of the National Center for Atmospheric Research (NCAR). NCAR is a major facility sponsored by the NSF under cooperative agreement no. 1852977. Z.Y. acknowledges funding for visits to the High Altitude Observatory from a Newkirk Fellowship awarded by NCAR. **Author contributions:** H.T. led the project. Z.Y. analyzed the data and generated the figures, tables, and movies under the supervision of H.T. H.T. and Z.Y. wrote and revised the manuscript. S.T. developed the UCoMP instrument, planned the observing sequences, and processed the raw data. Z.Y., X.L., and R.J.M. contributed the modified wave tracking method. S.G. developed the software for the calculation of observables from the MAS models. C.D. contributed to the development of the MAS models. All authors discussed the results and commented on the

manuscript. **Competing interests:** The authors declare no competing interests. **Data and materials availability:** UCoMP data are archived at https://mlso.hao.ucar.edu/mlso_data_calendar.php?calinst=ucomp; we used the datasets listed in table S1. The SUVI data were obtained from <https://www.ngdc.noaa.gov/stp/satellite/goes-r.html>; the files that we used are specified in the supplementary materials. The HMI synoptic magnetograms were obtained from the Joint Science Operations Center at http://jsoc.stanford.edu/ajax/lookdata.html?ds=hmi.Synoptic_Mr_720s; we used the files hmi.Synoptic_Mr.2254.fits, hmi.Synoptic_Mr.2258.fits, hmi.Synoptic_Mr.2259.fits, hmi.Synoptic_Mr.2260.fits,

hmi.Synoptic_Mr.2261.fits, and hmi.Synoptic_Mr.2262.fits. The source codes, output, and analysis scripts of our MAS models are archived at Zenodo (35). The PFSS model that we used for comparison was obtained in hierarchical data format from https://www.lmsal.com/solarsoft/archive/ssw/pfss_links_v2/Bfield_20220221_180328.h5. The source code of our modified wave tracking software is archived at Zenodo (36). **License information:** Copyright © 2024 the authors, some rights reserved; exclusive licensee American Association for the Advancement of Science. No claim to original US government works. <https://www.science.org/about/science-licenses-journal-article-reuse>

SUPPLEMENTARY MATERIALS

[science.org/doi/10.1126/science.ado2993](https://doi.org/10.1126/science.ado2993)
Materials and Methods
Supplementary Text
Figs. S1 to S4
Table S1
References (37–69)
Movies S1 to S3

Submitted 27 January 2024; accepted 2 September 2024
[10.1126/science.ado2993](https://doi.org/10.1126/science.ado2993)